ACS OMEGA

Open Access

http://pubs.acs.org/journal/acsodf

Article

FeNP@MIL-101(Fe)-Based Carbon Nanotube Composite for Energy Storage Applications

Hansa Mahajan, Arati Kumari Shah, Soomin Kim, and Seongjae Cho*

Cite This: *ACS Omega* 2024, 9, 24546−24557

Read Online

ACCESS | Metrics & More | Article Recommendations | Supporting Information

ABSTRACT: Metal−organic frameworks (MOFs) are of great interest for energy applications due to their high porosity, high charge storage capacity, and large number of active redox sites. It is important to enhance the performance of metal−organic frameworks through modification in order to increase their potential applications. Unique Fe nanoparticle (NP) in the Materials of Institute Lavoisier (MIL) series embedded in the carbon nanotube (CNT), FeNP@MIL-101(Fe)/CNT-based, nanocomposites have been synthesized using suitable hierarchical micromesoporous structures. These were fabricated by simple and straightforward solvothermal methods, and their electrochemical charge storage performance was investigated. The energy storage application using the FeNP@MIL −101(Fe)/CNT composite as a supercapacitor electrode was implemented for the first time. Various techniques were used to characterize this composite. It has excellent electrochemical properties when used as electrode material in 1 M KOH solution, including a high capacitance of up to 1305 F g^{-1} at 1 A g^{-1} and a long cycling stability of 95.7% capacitance retention after 10,000 cycles. Moreover, symmetric two-electrode electrochemical experiments showed that the composite achieved an energy density of 98.65 Wh kg^{-1} and a power density of 9000 W kg^{-1}, The combination of microporous and mesoporous structures, increased surface area, and higher electrical conductivity are the main reasons for the high performance. The integration of FeNP@MIL-101(Fe) with the CNT creates new ion diffusion pathways, improves the hierarchical pore properties, and exposes the FeNP@MIL-101(Fe) cluster to more redox active sites, which improves the charge storage performance.

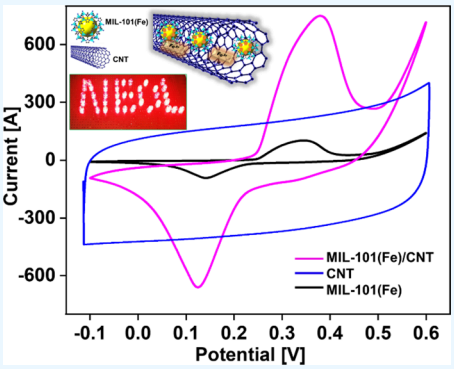

INTRODUCTION

Global energy consumption is rising, which has significantly increased the output of fossil fuels as the primary energy source. In parallel with the incessant effort made by the conventional electronic circuit-level approaches,[1] electrochemical energy storage (EES) has advanced considerably as the result of its great energy effectiveness, sustainability, and environmental sustainability.[2,3] EES devices contain capacitors, supercapacitors, batteries, and fuel cells since they have many ways to store charge. Supercapacitors have emerged as one of the most significant EES devices due to their great energy and power density, extended cycle constancy, and rapid charging process.[4,5] As per the International Energy Agency, supercapacitors are currently one of these leading possibilities for storing energy. Currently, three key applications for supercapacitors include vehicles, immobile energy storage, and portable power source.[6] Electrical double-layer capacitors (EDLC) and pseudocapacitors are the two primary types of supercapacitors based on how they store charge.[7] Whereas storing charge in pseudocapacitors uses the redox response of the synthesized material through the Faradaic method. On the other hand, charge storage in EDLC is accomplished through a high surface area of the active material and a slight charge separation. Various other kinds of carbon-based materials, including carbon nanotubes (CNTs), graphene, and activated carbon (AC) have been investigated for use in EDLC.[8−10] Pseudocapacitors are a different type of supercapacitors that may store charges by oxidizing and reducing both organic materials such as conducting polymers, inorganic materials, and transition metal oxides (TMOs) and metal−organic framework (MOFs).[11,12] Because of their high specific surface areas and controllable pore, metal−organic frameworks (MOFs) and their composites have recently been employed as precursors to produce porous carbon materials.[13,14] Metal−organic frameworks (MOFs), a novel type of energy storage materials, have shown a great deal of interest in the area of supercapacitors, which was primarily characterized by Yaghi et al. in 1995.[15] Inorganic components such as metal ions and multidentate organic linkers can be used to synthesize MOFs, which are porous and crystalline 3D materials.[16] The synthesis of Fe-MIL-101 was reported by Ferey and his group as one of the most significant discoveries in MOF-based chemistry.[17]

Received: January 19, 2024
Revised: April 19, 2024
Accepted: April 23, 2024
Published: May 28, 2024

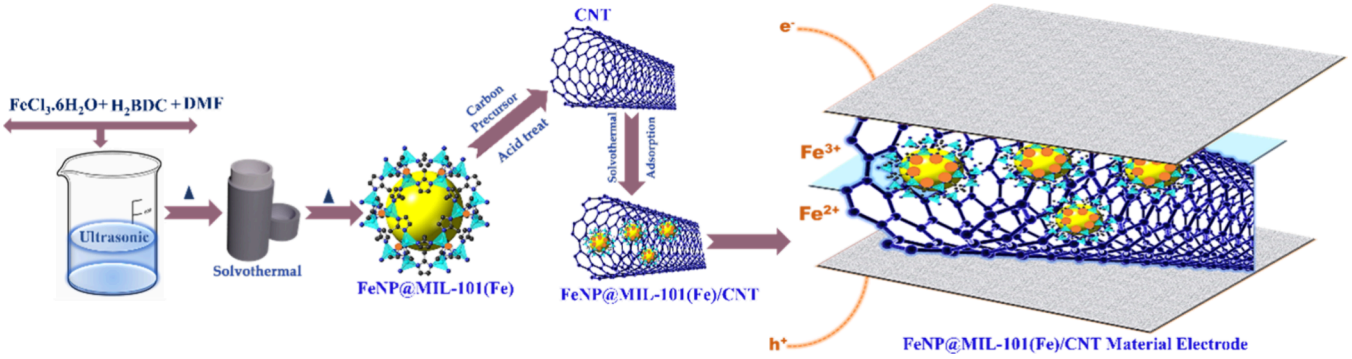

Figure 1. Schematic of the formation of the FeNP@MIL-101(Fe)/CNT composite supercapacitor.

Owing to their tunable shape, multifunctionality, great surface area, and abundance of pores, MOFs composed of metal centers and organic linkers with constant porosity are unique and interesting developments in current materials.[18] Energy storage, gas storage, and catalysis are just a few of the applications for which MOFs become promising materials.[19,20] The issue on nonconductivity of these materials has not yet been resolved. Scientists have concentrated on heating MOFs to transform them into useful materials as a means of overcoming this obstacle.[21] A single source for the synthesis of carbon-based materials, electroactive species, and transition metal oxides can be provided by heating the MOFs. Despite having a high capacitance, pseudocapacitors often have low cycle stability and limited rate capabilities.[22] The formation of a porous assembly and improvement of electrical conductivity associated with the active materials is then vital: these objectives can be accomplished by using electronically conductive elements like CNTs.[23] Because of its outstanding conductivity, mechanical properties, and ideally ultrahigh surface area, CNT got extensive attraction as a candidate for EDLC.[24,25] Researchers frequently investigate composites based on CNTs, during which some additional useful materials are included in demand to improve and utilize the appealing features of CNTs. Through a single step of MIL-101(Cr) and alcohol mix, Ullah et al. created Cr_2O_3-carbon nanocomposites that controlled graphite and pseudo-crystalline Cr_2O_3 nanoribbons.[26,27] They achieved a capacitance of 300 and 291 F g^{-1} at 0.25 F g^{-1} along with a capacitance retention of 90.5% over a period of 3000 cycles. The final electrode material (Cr_2O_3/C) similarly had a maximum Brunauer−Emmett−Teller (BET) surface area of 438 m^2 g^{-1}. Wang and co-workers described a straightforward mixture of Fe_3O_4-doped porous carbon nanorods.[28,29]

This study focuses on the demonstration of performance improvements expected by introducing FeNP@MIL-101(Fe) in the CNT matrix by preparing, characterizing, and electrochemically analyzing the FeNP@MIL-101(Fe)/CNT composite. The insertion of FeNP@MIL-101 inside the CNTs has the effect of preventing agglomeration of the nanoparticles, leading to better dispersion and stability of the material. This results in performance improvements and the durability of the composite material. Also, the encapsulation of FeNP@MIL-101 within the CNTs can provide benefits including an increase in effective surface area, improvement in electrical conductivity, enhanced stability, and higher charge storage capability. All of these contribute to better performances of the supercapacitor. This approach aims to enhance the electrochemical properties and performances of the nanocomposite-embedded electrode such as large specific capacitance (SC) and cyclic operation stability. Motivated by the primary studies in composing MOFs with carbon-based materials for supercapacitor application, herein we have aimed to prepare, characterize, and electrochemically analyze the FeNP@MIL-101(Fe)/CNT composite, to overcome the low conductivity of FeNP@MIL-101(Fe). The porous nature of MIL-101 provides a suitable environment for the formation and stabilization of Fe nanoparticles. The large effective surface area and pore volume of MIL-101 facilitate the nucleation and growth of Fe nanoparticles, resulting in the formation of the structure of the MOF. Here, the coordinatively unsaturated metal sites existing in MIL-101 act as the nucleation centers in forming the Fe nanoparticles. In this study, the electrochemical properties of the FeNP@MIL-101(Fe)/CNT composite electrode and bare FeNP@MIL-101 (Fe), and the CNT electrode material have been studied. The FeNP@MIL-101(Fe)/CNT nanocrystal assembly might bring higher performances in terms of high SC (1305 F g^{-1} at A g^{-1}), high-rate capability, and excellent cycling stability (capacitance retention of 95.7% after 10,000 cycles).

RESULTS AND DISCUSSION

The preparation of the FeNP@MIL-101(Fe)/CNT electrode material is schematically illustrated in Figure 1. MOFs represent a relatively new class of porous materials assembled from two main components: inorganic secondary building units (SBU) and organic linkers.[30] FeNP@MIL-101(Fe) SBU is composed of a carboxylate-bridged (H_2BDC), oxo-centered, trinuclear Fe^{3+} complex, and dimethylformamide (DMF). This specific SBU complex is a well-known topic in inorganic chemistry, and its electron density distribution and electrochemical properties have been previously reported.[31,32] During the synthesis of FeNP@MIL-101(Fe), H_2BDC as an organic linker, $FeCl_3{\cdot}6H_2O$, and *N*, *N*-DMF as a solvent was used. The chemical reaction occurs using a metal-based precursor and organic linker, *N*, *N*-dimethylformamide (DMF), forming a self-assembled FeNP@MIL-101(Fe) crystal structure.

Herein, DMF acts as a reducing agent of Fe^{3+} metal centers to Fe^{2+}. DMF plays an important role in MOF synthesis; thermally decomposing to release a base (dimethylamine) that can deprotonate the linker, consuming water (a source of O_2 and OH ligands found in SBUs) to produce a potential modulator (formic acid) and also potentially acting as a structure directing agent.[33,34] FeNP@MIL-101(Fe) crystals were incorporated into the CNT using a solvothermal technique. Although the CNT plays a major role in determining the characteristics of the composite material, the

https://doi.org/10.1021/acsomega.4c00590
ACS Omega 2024, 9, 24546−24557

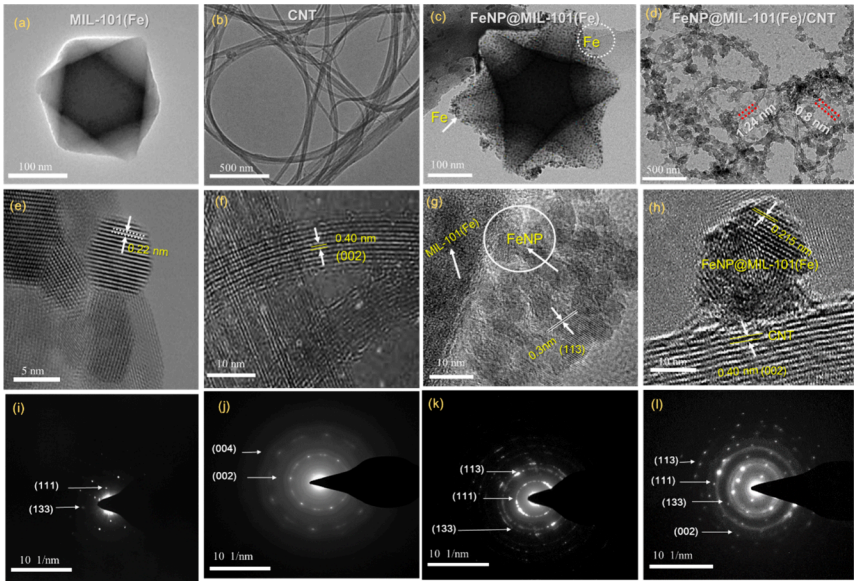

Figure 2. (a–d) Transmission electron microscopy (TEM) images. (e–h) High-resolution TEM (HR-TEM) images and lattice fringes. (i–l) Selected-area electron diffraction (SAED) patterns of MIL-101(Fe), CNT, FeNP@MIL-101(Fe), and FeNP@MIL-101(Fe)/CNT composites.

presence of FeNP@MIL-101 has several effects of further enhancing its electrochemical performances. First, the insertion of FeNP@MIL-101 in the CNT matrix provides additional active sites for electrochemical reactions. The existence of Fe nanoparticles allows for redox reactions to take place on the surface, accelerating electron transfer and enhancing the electrochemical activity of the system. Second, the FeNP@MIL-101 particles in the CNTs can improve the reaction stability to the electrode material. The nanoparticle-associated CNTs offer protection to the Fe nanoparticles, preventing either agglomeration or detachment of the nanoparticles during electrochemical reactions. This stability ensures the long-term performance and durability of the electrode material.

MIL-101 series MOFs have similar zeolite topology but different surface morphology, density, and pore sizes. Most of the MIL series materials are composed of Cr(III), Fe(III) and Al(III) metal ion clusters. The inorganic building unit of MIL-101(Fe) is a secondary building unit (SBU) composed of a carboxylate-bridged (H_2BDC), oxo-centered, trinuclear Fe^{3+} complex and DMF. This specific SBU complex is a well-known topic in inorganic chemistry.[31] The main difference between MIL-101(Fe) and MIL-101 is the type of metal centers present in the metal organic framework. MIL-101 is a type of metal–organic framework (MOF) that consists of metal oxide clusters as the inorganic building unit, specifically octahedral $\{M_6O_8\}$ clusters. These clusters are connected by organic linkers to form a 3D porous framework structure. MIL-101(Fe) is a variant of MIL-101 that is specifically constructed using Fe (III) ions as the metal ions in the building units. The inorganic building unit of MIL-101 is $[Fe_3O(O_2C{-}C_6H_4{-}CO_2)_3]$. This unit is connected by organic linkers to form the overall structure of the MOF. During the synthesis of MIL-101(Fe), Fe nanoparticles are formed through a process called "autoreduction". This process involves the reduction of Fe(III) to Fe(II) by organic ligands in MIL-101(Fe). As a result, Fe(II) ions are released and they cluster together to form Fe nanoparticles. These nanoparticles are then encapsulated within the MIL-101(Fe) framework, resulting in the final product.[11]

In the composite structure, carbon nanotubes are used as a strong anchor, whose surface can be simply altered via carboxyl functionality, easing the completion of the homogeneous evolution of FeNP@MIL-101(Fe) and enhancing the conductivity, which can supply a small ionic diffusion impedance. CNTs can be a current-collecting source to reduce the route distance of electron collection/transport and the interaction of CNTs and the FeNP@MIL-101(Fe) MOF. This can also buffer the massive volume shift of the active sites during long-term cycling. As the electrode material, the composite of the FeNP@MIL-101(Fe)/CNT matrix coupled with the CNT, in which CNTs act as an extremely conductive medium for quick electron transfer, behaves as a collecting current source. However, FeNP@MIL-101(Fe) adheres to the surface of CNTs and cannot control the aggregation of CNTs to deliver an electrochemically dynamic surface, which significantly expands the wettability of electrolytes because of the many functional groups.[35] Lab-synthesized CNTs are still hydrophobic, so to make CNTs hydrophilic, the surface of CNTs needs functionalization by hydrophilization using nitric acid during the synthesis of CNTs.[36,37] The nitric acid used for the hydrophilization process can reduce impurities on the CNTs and improve the wettability. In that way, the ions contained in the electrolyte easily enter the CNT pore and stick to the inner surface, so that it can increase the capacitance.

Characterization of Materials. The surface morphologies of MIL-101(Fe), CNT, FeNP@MIL-101(Fe), and FeNP@MIL-101(Fe)/CNT composites were examined by transmission electron microscopy (TEM), the results of which are shown in Figure 2a–l. Figure 2a shows the low magnification of TEM images revealing that MIL-101(Fe) is an octahedral nanocrystal consisting of an average edge length of ∼20–30 nm. The surface of MIL-101(Fe) was smooth and showed similar morphology to previously reported literature.[38] Meanwhile, the morphology of carbon nanotubes with dense tube-like shapes with a diameter of 0.8 to 1.8 nm is shown in Figure 2b.

Likewise, the FeNP@MIL-101(Fe) crystals had concave regular octahedron morphology with an average diameter of

https://doi.org/10.1021/acsomega.4c00590
ACS Omega 2024, 9, 24546–24557

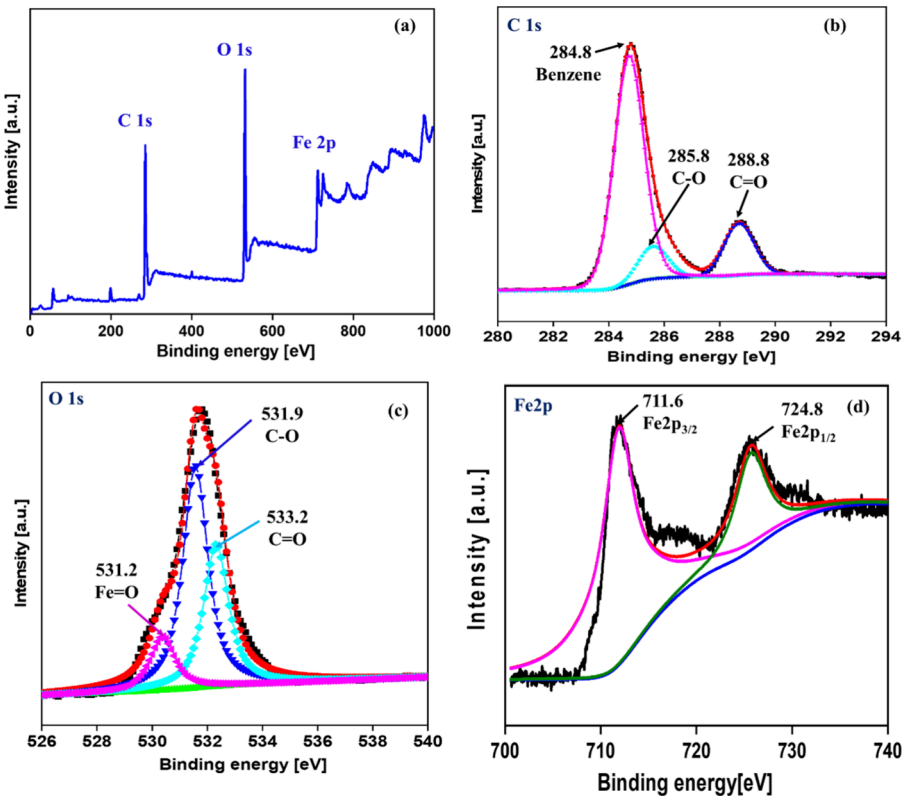

Figure 3. X-ray photoelectron spectra from (a) full survey, (b) C 1s, (c) O 1s, and (d) Fe 2p of the FeNP@MIL-101(Fe)/CNT composite.

100 nm which corresponds with the MOFs matrix. The surface was smooth and uniformly embedded with Fe particles encapsulated therein (black in color in Figure 2c) and the size and morphology did not change, which is consistent with MIL-101(Fe) nanocrystals. It can be observed that the Fe decoration of not only the outermost surface of the MOF particles with a mean size of several hundred nanometers but also a substantially large portion of their internal pores. Moreover, the assembly of the FeNP@MIL-101(Fe)/CNT composite introduces a mixed characteristic of FeNP@MIL-101(Fe) crystal winding inside the tube-like structure. The FeNP@MIL-101(Fe)/CNT composite in Figure 2d is clearly smaller, with a typical size of 10 nm compared to FeNP@MIL-101(Fe) owing to the strengthening and implantation of CNT. The high-resolution morphology in Figure 2e reveals that the lattice fringes of MIL-101(Fe) are 0.22 nm, representing the (111) plane. Moreover, the crystallinity of CNTs with lattice fringes is 0.40 nm, which corresponds to the (002) plane, as shown in Figure 2f. The embedded Fe particles in FeNP@MIL-101(Fe) indicate high crystallinity with an interplanar spacing of 0.3 nm corresponding to the (113) planes of Fe particles (Figure 2g). Figure 2h clearly illustrates the open-ended features of the CNT and the FeNP@MIL-101(Fe) crystal encapsulated within these nanotubes. Here, the growth of the FeNP@MIL-101(Fe) MOF is restricted by the dimensions of the CNTs, affording a crystal size of 2.2 ± 0.2 nm. Additionally, the encapsulated FeNP@MIL-101(Fe) crystals were uniformly distributed in the CNTs without severe aggregation. The highly crystalline nature of the FeNP@MIL-101(Fe) crystal is manifested by the lattice spacing corresponding to the (111) plane. The morphology was unaffected, even after encapsulation of the CNTs. MOFs have a self-assembling process and porous TMOs because of the oxidation of the metal ions because they consist of metal centers coordinated with organic linkers. The selected-area electron diffraction (SAED) pattern confirmed the crystal configuration of the as-synthesized materials (Figure 2i–l). The selected-area electron diffraction (SAED) pattern with Debye–Scherrer rings was observed in the (113), (111), (133) planes for FeNP@MIL-101(Fe) which shows the highly crystalline structure (Figure 2k) whereas (113), (111), (133), and (002) crystal planes of the FeNP@MIL-101(Fe)/CNT composite (Figure 2l), representing polycrystalline properties, which matches the X-ray diffraction (XRD) result.[39] The elemental analysis results in comparison between FeNP@MIL-101(Fe) and FeNP@MIL-101(Fe)/CNT compounds from energy-dispersive X-ray spectra (EDS) are presented in Figure S1a,b in the Supporting Information (SI). These analyses indicate that the main elements C, O, and Fe were properly and homogeneously spread throughout the composite (Figure S1b), where C was derived from the CNT precursor and Fe and O were derived from the MIL-101(Fe) precursors and organic linkers used to synthesize the composite. Fe in the particles was mainly in the form of atoms, and most of the Fe atoms were concentrated on the confined particles. Results in the EDS also show that the carbon element (weight percentage) in the case of composite is much higher than FeNP@MIL-101(Fe) which clearly shows that the carbon elements are from CNT. Furthermore, elemental mapping images were used to confirm the metallic nanoparticles in the FeNP@MIL-101(Fe)/CNT composite as shown in Figure S2 in SI. The use of elemental mapping images can provide additional information on the distribution of elements within the material, which can help confirm the presence of specific elements and their relative concentration. Figure S2 in SI shows the elemental mapping images obtained

https://doi.org/10.1021/acsomega.4c00590
ACS Omega 2024, 9, 24546−24557

from the Fe@MIL-101(Fe)/CNT composite, which can be used to confirm the distribution of Fe, C, and other elements in the composite.

The results show that we successfully synthesized a FeNP@MIL-101(Fe)/CNT composite with a porous assembly and homogeneous structure. CNT and FeNP@MIL-101(Fe) synergistically interacted to enhance the electrochemical characteristics. Also, it is explicitly revealed that FeNPs are necessary for electrochemical measurements for their contributions in several aspects: The Fe NPs act as conductive additives, improving the electrical conductivity of the electrodes. This facilitates the efficient transfer of charges during the charging and discharging processes. Given that the number of charges that can be stored in a capacitor is fixed, how fast charging and discharging can be allowed in the unit time provides a larger capacitance of the structure by the mathematical definition of capacitance. The catalytic role of Fe NPs, particularly concerning redox activities, has an effect of enhancing the electron transfer kinetics during the redox reactions within the battery system. It practically helps improve the overall system stability and charging/discharging rates of the battery. More specifically, the Fe NPs act as catalysts by facilitating the redox reactions at the electrode−electrolyte interface, promoting faster electron transfer and reducing energy loss during the process. The accelerated redox reactions, based on the faster charge storage and release processes, are closely correlated with the obtainment of a larger capacitance. Also, Fe NPs provide an enlarged effective surface area, by which a larger number of active sites for ion adsorption and desorption are formed. The large effective surface area and unique electronic properties of the Fe NPs make them effective catalysts in the redox reactions and eventually lead to improvement in the battery performances. Recalling the simple relation between area and capacitance, it is assured that a larger energy storage capacity can be acquired by the effective area enlarged in a given volume. Fe NPs can enhance the stability and durability of the electrode material. Along with the surveyed enhancements in the electrochemical performances, Fe NPs themselves can play a role as a physical passivation layer that minimizes electrode corrosion.

In order to analyze the surface chemistry of FeNP@MIL-101(Fe)/CNT composite, XPS was conducted as shown in Figure 3a,b.[32,40] In the full spectrum of FeNP@MIL-101(Fe)/CNT composite, peaks representing C, O, and Fe elements were illustrated in Figure 3a. As shown in Figure 3b, the C 1s peak can be divided into three peaks at 284.8 285.8, and 288.8 eV which represent the carbon atoms bond (C−C) and carbon organic linkers (C−O and O−C═O) of FeNP@MIL-101(Fe). The O 1s peaks can be convoluted into three peaks of 531.2, 531.9, and 533.2 eV, which are related to the oxygen atoms in Fe−O bonds, C−O linkers, and C═O linkers, as shown in Figure 3c. For the Fe 2p spectrum, four peaks were observed among them, and peaks at 711.6 and 724.8 eV were characteristic peaks of Fe $2p_{3/2}$ and Fe $2p_{1/2}$, respectively, proving the existence of F−O bonds in the FeNP@MIL-101(Fe)/CNT composite as depicted in Figure 3d.

The FT-IR pattern (Figure S3a) of FeNP@MIL-101(Fe) presented distinct peaks at 752, 1022, 1398, 1580, and 1682 cm^{-1}, indicating the C−H bond in benzene.[41] Peaks 1398 and 1580 cm^{-1} suggested the existence of a carboxyl (−COO−) peak. Peak 1682 cm^{-1} originated from C═O bonds of carboxyl. These peaks indicated the existence of ligand dicarboxylate linkers in FeNP@MIL-101(Fe). However, in the case of CNT, the peak at 1600 cm^{-1} originated from C═C which is the strong carbon bonding present in the CNT. Moreover, the aliphatic compounds, sp^3 hybridized carbon absorption normally occurs at a wavenumber lower than 3000 cm^{-1}, which is the stretching vibration of the C−H group that has given rise to the appearance of peaks at the wavenumber around 2890 cm^{-1}. After the addition of CNT, no evidence of shifting of the characteristic peak was observed. The XRD spectra of FeNP@MIL-101(Fe) and FeNP@MIL-101(Fe)/CNT composite are illustrated in Figure S3b. Reported literature shows the simulated XRD pattern of MIL-101(Fe) has characteristic peaks at 2θ = 8.4°, 9.7°, 16.4°,[42,43] whereas our sample FeNP@MIL-101(Fe) has four characteristic peaks at 2θ = 8.4°, 9.7°, 19.7°, and 21.6°, respectively, hence it is clearly showing Fe particles are encapsulated in the crystal of MIL-101(Fe). Whereas FeNP@ MIL-101(Fe)/CNT composite contained similar patterns, indicating that the addition of CNT (25.5° and 42.2°) did not obstruct the generation of the MIL-101(Fe) crystal. However, the intensities of these peaks gradually decreased when CNT was added, which may be due to the partial distortion of the FeNP@MIL-101(Fe) framework and the winding of CNT. Figure S3c shows the Raman spectra of the CNT and FeNP@MIL-101(Fe)/CNT composite. Typical Raman bands of carbon nanotubes are radial breathing mode (RBM),[44] D band, and G band. The RBM peak appears in the range from 100 to 300 cm^{-1} as shown in Figure S3c. There were several RBM peaks in the spectrum, indicating the different distributions of diameters. As a result, the CNT diameters ranged from 0.8 to 1.8 nm. In particular, distinct peaks appear at 264.9, and 298.3 cm^{-1} as confirmed by the diameter corresponding to 1.24 and 0.8 nm of CNTs. The G band peak around 1590 cm^{-1} is derived from the in-plane vibration of the six-membered ring carbon structure. Defects and sp^3 hybridized carbon atoms give rise to a "D" band centered at 1345 cm^{-1}, the height of which is inversely related to the nanotube quality. These results show a higher graphitic degree, which improves the electrical conductivity and therefore induces charge transfer. In contrast, the spectra of the FeNP@MIL-101(Fe) crystals correspond to those of the organic ligands. The peak at 1178 cm^{-1} is attributed to the C═O moiety in the carboxylic bond and the C−C bond in the benzene ring. Additionally, the peak at 861 cm^{-1} is attributed to vibrations of the H−C bonds and the benzene ring, indicating that the CNTs were successfully tailored in the FeNP@MIL-101(Fe)/CNT compounds. The intensity of the characterization Raman peaks of MOF and CNT can be used to estimate their respective amounts in the composite as shown in Figure S3c. The previous difficulty in distinguishing the FeNP@MIL-101(Fe) from the CNT walls by TEM can be relieved by these characterization techniques, XRD (Figure S3b) and Raman spectroscopy (Figure S3c), which were utilized to confirm the presence of the nanoparticles inside the CNTs. In the FeNP@MIL-101(Fe)/CNT composite, the characterization peak for CNT is typically overserved at around 1580 nm^{-1}, while the characterization peaks of FeNP@MIL-101(Fe) are typically observed at around 800 nm^{-1} and 1625 nm^{-1}. To estimate the relative amount of MOF and CNT, in the composite, the intensities of the characteristic peaks can be compared. The ratio of the peak heights can be used to estimate the relative amount of MOF and CNT in the composite. If the intensity of the Raman peak at 1625 nm^{-1} for FeNP@MIL-101(Fe) is twice that of Raman peaks at 1580

https://doi.org/10.1021/acsomega.4c00590
ACS Omega 2024, 9, 24546−24557

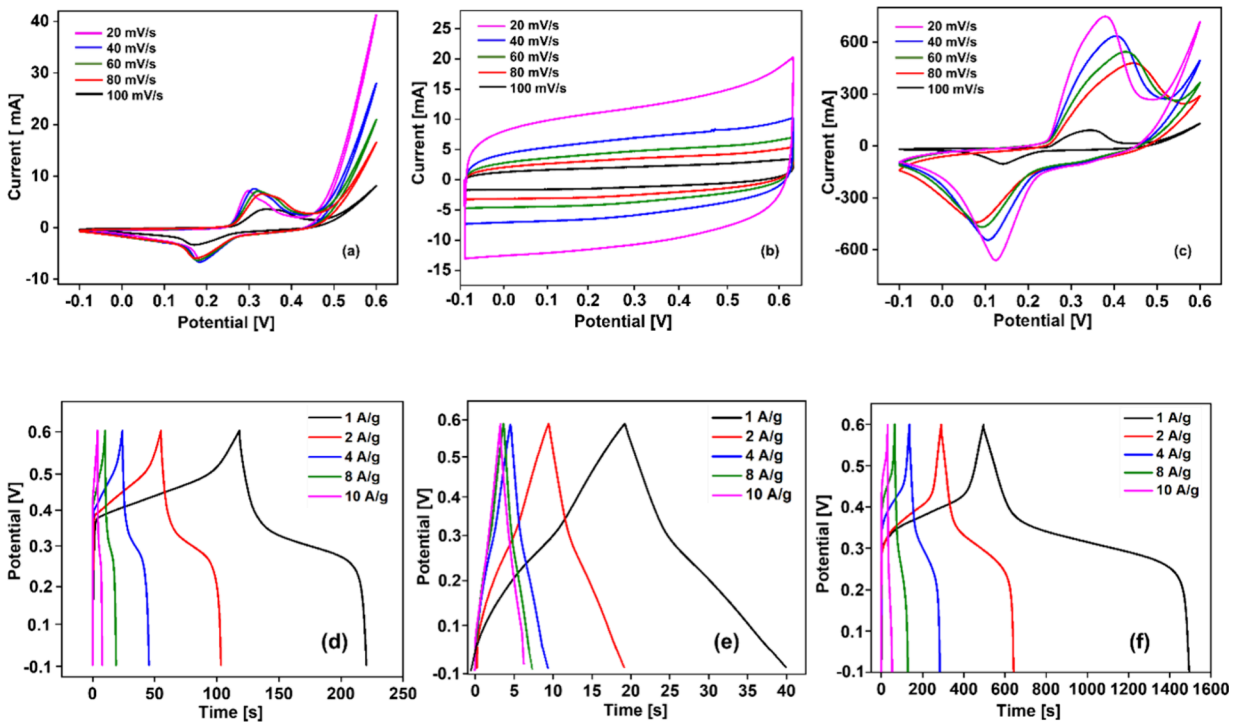

Figure 4. Electrochemical characterization: (a−c) cyclic voltammetry curves obtained at different scan speeds (20−100 mV s^{-1}) and (d−f) galvanostatic charge−discharge curves of FeNP@MIL-101(Fe), CNT, and FeNP@MIL-101(Fe)/CNT electrodes at different current densities.

nm^{-1} for CNT then the ratio of MOF to CNT in the composite would be approximately 2:1. Thus, Raman spectroscopy techniques have been used to obtain an estimation of the amount of MOF present in the composite. Thermogravimetric analysis (TGA) was used to determine the stability of the FeNP@MIL-101(Fe) crystals and FeNP@MIL-101(Fe)/CNT composites, the results of which are shown in Figure S3d. FeNP@MIL-101(Fe) crystals have initial weight loss between 50 to 440 °C as a result of moisture evaporating from the pores and free terephthalates being eliminated (Fe). Then, the large weight loss in the temperature range of 440 to 750 °C, is due to the breakdown of interconnected organic ligands. Finally, the framework collapses at about 800 °C. In comparison to pure FeNP@MIL-101(Fe), the FeNP@MIL-101(Fe)/CNT composite generally demonstrated the same thermal deterioration mechanism (Fe). Owing to the presence of CNT, FeNP@MIL-101(Fe)/CNT did, however, exhibit a minor weight loss at temperatures around 750 °C.[44]

Figure S4 illustrates the surface area of FeNP@MIL-101(Fe), CNT, and FeNP@MIL-101(Fe)/CNT composites measured by using the BET method. The FeNP@MIL-101(Fe) crystal exhibits high nitrogen-saturated adsorption, presenting a type-I adsorption−desorption isotherm. They typically possess a microporous assembly. The adsorption−desorption characteristics changed after encapsulation, and the FeNP@MIL-101(Fe)/CNT composite exhibited a typical type-IV adsorption−desorption isotherm that displayed a mesoporous structure [4,38.] Reported MIL-101(Fe) at ambient conditions is approximately adsorbed 2.15 cm^3/g of N_2 and our sample shows the N_2 adsorbing capacity at 0.6 cm^3/g as shown in Figure S4,[45,46] which shows iron incorporated, thus altering porosity. MIL-101(Fe) is less mesoporous, hence to increase its porosity and surface, CNT was used. In comparison to FeNP@MIL-101(Fe) (76.7 m^2 g^{-1}) and CNTs (287.5 m^2 g^{-1}), the surface area of the FeNP@MIL-101(Fe)/CNT composite is extremely high (1488.580 m^2 g^{-1}), as shown in Figure S4 with the legends (i−iii). The incorporation of CNT into the composite material and FeNP@MIL-101(Fe) structure, which reduced the number of pores per unit mass, contributed to the increase in the surface area. Additionally, the presence of CNT makes it simple for organic ligands to interact with Fe^{3+} ions, and substantially increases the surface area of FeNP@MIL-101(Fe)/CNT composites.

■ ELECTROCHEMICAL PERFORMANCE

Cyclic voltammetry (CV) and galvanostatic charge−discharge (GCD) were employed to measure the supercapacitor characteristics of FeNP@MIL-101(Fe), CNT, and FeNP@MIL-101(Fe)/CNT composite electrodes, in 1-M KOH solution. For the electrodes, the prepared Nickel form was used as a substrate and was applied for a binder-free electrode for the supercapacitors. All of the electrochemical properties were measured in the two-electrode cell using a 1-M KOH aqueous electrolyte medium. Although KOH is not the only aqueous electrolyte solution that can be prepared for the experimental evaluation, it is widely accepted as one of the most appropriate platforms for supercapacitor operations owing to its cost-effectiveness, high conductivity, relatively wide operating voltage window, and higher energy density. Also, instead of using an arbitrary concentration of KOH, 1-M KOH was used to make it easier to quantify a series of performance indices in a normalized manner. While using nickel form, KOH is used as an electrolyte because of its great ionic conductivity and great mobility of the OH^- anion in H_2O, for one of the reasons addressed above.

Figure 4a−c presents the CV curves of the FeNP@MIL-101(Fe), CNT, and FeNP@MIL-101(Fe)/CNT composite electrodes, measured at multiple scan speeds ranging from 20 to 100 mV s^{-1} and the potential window ranging from −0.1 to

https://doi.org/10.1021/acsomega.4c00590
ACS Omega 2024, 9, 24546−24557

+0.6 V. For more details, CV characteristics of CNT remained ideal and rectangular in shape even at a higher scan speed of 100 mV/s, demonstrating CNT electrodes show double-layer capacitor performance and serve as good current collectors to provide conductive paths. However, the FeNP@MIL-101(Fe) and FeNP@MIL-101(Fe)/CNT composites have redox peaks that correspond to the surface redox reaction between Fe^{3+} and Fe^{2+} indicating its faradic behavior for the charge storage mechanism. Moreover, the CV curve of the FeNP@MIL-101(Fe)/CNT composite shows peak current is higher than the FeNP@MIL-101(Fe) and CNT electrodes. It is evident that the charge storage behavior of FeNP@MIL-101(Fe)/CNT composite results from the synergistic effects between the two components and the increased surface area of the composite provides more accessible sites for the intercalation and/or absorption of electrons and ions in the electrolytes. An increase in scan speed resulted in a significant decrease in charge transfer resistance between OH^- and the electrode; cathodic and anodic peaks shifted in the negative and positive directions. The peak current increased suggesting a rapid redox reaction, especially anions diffusion and charge transfer of the composite. The FeNP@MIL-101(Fe) has the valency Fe (III), and Fe (III) transforms to Fe (II) in the KOH medium. Therefore, it can store the charge as follows:

$$\mathrm{Fe(III)} + \mathrm{OH^-} = \mathrm{Fe(II)}$$

From the CV measurement of FeNP@MIL-101(Fe)/CNT, the faradaic reaction on the Fe^{3+} sites may take place as follows:

$$\mathrm{MIL - FeOOH + H_2O + e^- \leftrightarrow MIL - Fe(OH)_2 + OH}$$

$$\mathrm{MIL - Fe^{3+} + OH^- + e^- \leftrightarrow OH^- - (MIL - Fe^{2+})}$$

Figure S5 shows that the FeNP@MIL-101(Fe)/CNT electrodes are responsible for their remarkable performance of supercapacitors because of the following: (1) the chemical stability of CNT, which can help as stable support and provide an active site for FeNP@MIL-101(Fe). (2) The mesoporous structure of FeNP@MIL-101(Fe)/CNT composite ensures to provide sufficient interaction with the electrodes and the electrolyte which improves the performance of the supercapacitors. (3) It can be seen that the redox peak has occurred and shows faradic behavior due to the standard reduction of Fe ions in an aqueous medium along with the redox reaction of Fe^{3+} to Fe^{2+} which is the reaction of active materials.[47−51] GCD curves at different current densities (1−10 A g^{-1}) are shown in Figure 4d−f to determine the charge capacity of the electrode materials FeNP@MIL-101(Fe), CNT, and FeNP@MIL-101(Fe)/CNT. The good reversible and capacity performance of the CNT electrode is indicated by the straight-line and triangular forms of the charge−discharge characteristics. Based on the CV curves, the charge−discharge curves of the FeNP@MIL-101(Fe) and FeNP@MIL-101(Fe)/CNT electrodes displayed well-marked voltage plateaus, which suggests the nature of the redox reaction within the electrode and electrolyte.[41] The charge−discharge period of the FeNP@MIL-101(Fe)/CNT composite was longer than those of the CNT and FeNP@MIL-101(Fe) electrodes, indicating the high SC. One possible reason for the high capacitance is that a large effective surface area works in favor of ion and electron transfer in the anode and cathode. Another important reason is the fast ion-electron transfer in the FeNP@MIL-101 (Fe)/CNT composite. SC,[42] as obtained from the discharge curve, is based on eq 1.

$$C = I\Delta t/m\Delta V \tag{1}$$

where C is the measured SC, I is the discharge current, Δt is the discharge time, m is the active mass, and ΔV is the potential change in the discharge.

The energy and power densities were further calculated from the following equations: The energy density of a supercapacitor is the amount of energy per mass that can be obtained from a charged supercapacitor in units of Wh/kg. The higher the energy density becomes, the longer electrical power can be supplied for the same mass.

$$E = \frac{CV^2}{2m} \tag{2}$$

Here, E is energy density, V is the rated voltage in volts, C is the actual measured capacitance in farads, and m is the mass of the electrode.

The power density of a supercapacitor is the maximum electrical power per unit mass that can be obtained from a charged supercapacitor in units of W/kg. It is normally calculated from the internal resistance and rated voltage. The higher the power density becomes, the larger the instantaneous current can be efficiently obtained.

$$P = \frac{1}{2}\frac{V^2}{R \times m} \tag{3}$$

P is power density, V is the rated voltage in the unit of volts, R is the actual measured internal resistance in the unit of ohms, and m is the mass of the electrode.

EDLC behavior refers to the energy storage mechanism based on electrostatic charge separation at the interface between the electrode and the electrolyte. In this mechanism, the electric double layers are formed at the electrode−electrolyte interface, where the charge is stored through the ion adsorption and desorption processes. This mechanism provides fast charging and discharging capabilities with a high power density. The faradic redox reaction involves the reversible transfer of electrons between the electrodes and the redox-active species in the electrolyte. In this mechanism, the redox-active species undergoes a chemical reaction, resulting in the storage of charge. This mechanism allows a higher energy density compared to the EDLC behavior but usually shows slower kinetics. In this sense, the FeNP@MIL-101(Fe)/CNT composite combines EDLC behavior and a faradic redox reaction, and achieves a synergistic effect in storing energy. The FeNP embedded in the MIL-101(Fe) MOF provides redox-active sites for the faradic redox reaction. The CNT framework serves as a conductive network, facilitating electron transport and enhancing the overall conductivity of the composite. The synergistic effects arise from the combination of these mechanisms. The EDLC behavior provides rapid charge and discharge rates (faster kinetics), contributing to the high power density of the composite. At the same time, the faradic redox reaction involving the FeNP enables a higher energy density and improves the overall energy storage capacity. The presence of FeNP@MIL-101(Fe) and CNT in the composite enhances the electrochemical performance by increasing the effective active surface area, promoting electron transfer, and improving the stability of the electrode material.

https://doi.org/10.1021/acsomega.4c00590
ACS Omega 2024, 9, 24546−24557

The mass of both electrodes in the supercapacitor cell was used for calculating the current density and SC values. The mass loading of the FeNP@MIL-101(Fe)/CNT composite has been calculated at around 4.0 mg for a 1-cm^2 electrode area. The SC of FeNP@MIL-101(Fe), CNT, and FeNP@MIL-101(Fe)/CNT electrodes at different current densities of 1, 2, 4, 8, and 10 A g^{-1} are depicted in Figure 5a. At a current density of 1 A g^{-1}, the FeNP@MIL-101(Fe)/CNT electrode has an SC of 1305.72 F g^{-1}, higher than those of the FeNP@MIL-101(Fe) electrode (300.42 F g^{-1}) and CNT (178.5 F g^{-1}). Therefore, the integration of the CNT could improve the SC of the composite electrode. The low activation energy of electron transport among the cations may be the reason for the capacitive performance. As the current density increased from 1 to 10 A g^{-1}, the capacitance of the FeNP@MIL-101(Fe)/CNT electrode decreased from 1305.72 to 935.41 F g^{-1}, as shown in Figure 5a. Additionally, at high current densities, the active material has limited reaction time, which results in a decrease in SC. In contrast, FeNP@MIL-101(Fe)/CNT obtained a higher SC than that of the FeNP@MIL-101(Fe) electrode (300.42−182.24 F g^{-1}, Figure 5a) and the CNT electrode (178.5−88 F g^{-1}, Figure 5a) at a given current density. This is because the active material and electrolyte gradually penetrate the internal area of the electrode, where they activate additional sites and produce an excellent electrochemical performance.[52] The conductivities of the materials making up the battery structure, such as electrolytes and electrodes, play a crucial role in determining the efficiency and overall performance. For measuring them, electrochemical impedance spectroscopy (EIS) was adopted in this work, which is a widely used technique to assess the conductivities of these materials. By measuring and optimizing the conductivities in the individual components, energy storage capabilities, charge/discharge rates, and overall efficiency can be substantially improved. Figure 5b shows the Nyquist plot of FeNP@MIL-101(Fe), CNT, and FeNP@MIL-101(Fe)/CNT electrodes in 1-M KOH. Each impedance spectrum has a semicircle arc and a straight line. The high-frequency arc corresponds to the charge transfer limiting process and results from the double-layer capacitance (C_{dl}) in parallel with the charge transfer resistance (R_{ct}) at the contact interface between the electrode and the electrolyte solution. R_{ct} can be directly measured as the semicircle arc diameter. The values of R_{ct} for FeNP@MIL-101(Fe), CNT, and FeNP@MIL-101(Fe)/CNT electrodes are 6.3, 1.8, and 0.7 Ω, respectively, indicating that the incorporation of CNT improves the charge transfer performance of the FeNP@MIL-101(Fe)/CNT composite electrode. The equivalent series resistance (ESR) can be obtained from the X-intercept of the Nyquist plot, which determines the rate at which the supercapacitors can be charged/discharged. The ESR values shown in Figure 5b are 6.3 Ω for the FeNP@MIL-101(Fe) electrode, 1.8 Ω for the CNT electrode, and 0.7 Ω for the FeNP@MIL-101(Fe)/CNT composite electrode, respectively, which demonstrates that the addition of CNT modifies the conductivity of the composite. In addition, at low frequencies, the impedance plot should theoretically be a vertical line, which is parallel to the imaginary axis. In fact, the low-frequency straight line always departs from that expected with a slope angle close to 90° due to the existence of a "constant phase element". The straight lines close to 90° indicate a pure capacitive behavior and low diffusion resistance of ions in the structure of the electrodes. The more vertical the curve is, the more closely the supercapacitors behave as an ideal capacitor.[53,54] The filled CNTs in the composite electrode provide good conductive paths and reduce the charge-transfer resistance, and all of these contribute to the improved electrochemical performance of the FeNP@MIL-101(Fe)/CNT composite.

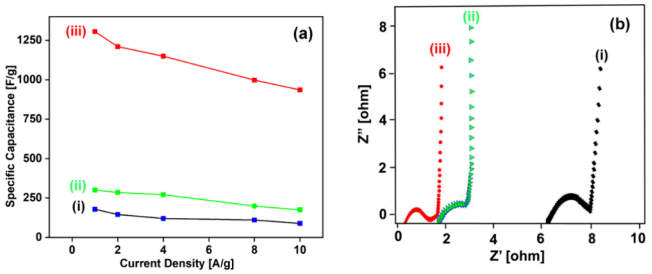

Figure 5. Energy storage characterization of the composite-based device. (a) Specific capacitance measurement and (b) electrochemical impedance spectroscopy results: (i) FeNP@MIL-101(Fe), (ii) CNT, and (iii) FeNP@MIL-101(Fe)/CNT electrodes.

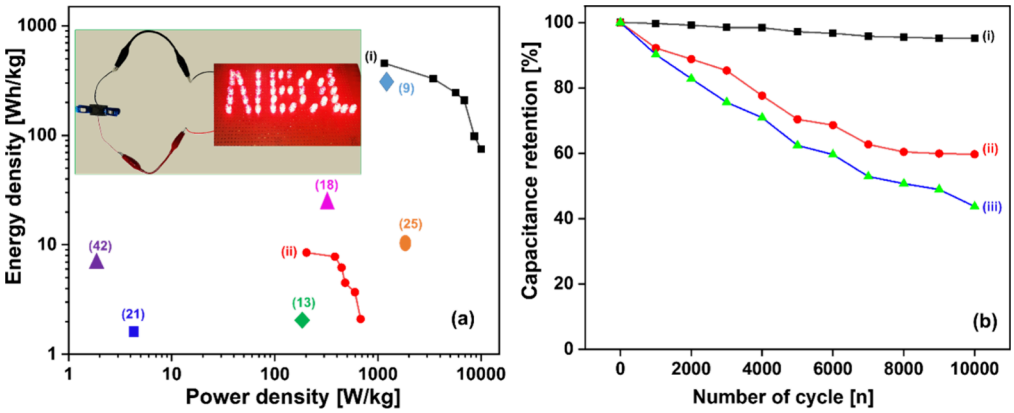

Figure 6. Performance of the FeNP@MIL-101(Fe)/CNT composite electrode material supercapacitor. (a) Ragone plot of the symmetric device showing the energy and power densities of the (i) FeNP@MIL-101(Fe)/CNT composite and (ii) FeNP@MIL-101(Fe) electrode. The performance is compared against previous reports (symbols with reference numbers). The inset shows a photograph of lit-up LEDs powered by a supercapacitor device with a FeNP@MIL-101(Fe)/CNT composite electrode. (b) Cyclic stability analysis of (i) FeNP@MIL-101(Fe)/CNT composite electrode, (ii) FeNP@MIL-101(Fe) electrode (iii) CNT electrode.

https://doi.org/10.1021/acsomega.4c00590
ACS Omega 2024, 9, 24546−24557

Figure 6a (legends i–ii) shows the Ragone plot of electrode materials for the supercapacitor device, and it is a very convenient way to show the energy density and power density. Based on eqs 2 and 3, the energy density (E) and power density (P) of the supercapacitors were evaluated. Figure 6a shows a Ragone plot of the energy and power densities of the FeNP@MIL-101(Fe)/CNT electrode. The energy density of a prepared supercapacitor is the amount of energy per unit of mass that can be achieved from a charged device, and it can be measured in Wh kg^{-1}. The higher the energy density, the longer electrical power can be supplied for the same mass (kg). To examine the power density of the prepared supercapacitor is the maximum electrical power that can be obtained from the charged device per unit of mass, and it is measured in W kg^{-1}. It is normally calculated from the internal resistance and the rated voltage. The higher the power density, the larger the instantaneous current that can be efficiently obtained. The FeNP@MIL-101(Fe)/CNT device displayed an excellent energy density of 9000 Wh kg^{-1} and power density of 98.65 W kg^{-1} at a constant current density of 1 A g^{-1} which are higher than those of the CNT electrode; Figure 6a. The power and energy densities have been enhanced due to its composite structure. CNT has high electric conductivity, and FeNP@MIL-101(Fe) has rapid access of ions to redox sites. In this manner, these composite materials represent an attractive class since they feature a large number of active sites and can spontaneously be intercalated by ions and electrons and therefore fill the active sites with ions the right way but to be fast and scalable. These electrochemical performances are better than those of carbonized MOF and biocarbon.[47,55] The electrochemical performances of the symmetric devices, including their SC, energy, and power, are compared in Table S1 in SI. Currently, energy density development is achieved by increasing the SC of electrodes with pseudocapacitive materials.[53] A two-electrode system was used to evaluate the capacitive performance of the supercapacitors. The positive and negative electrodes of the symmetric supercapacitor were made of FeNP@MIL-101(Fe)/CNT composite electrodes. The device depicted in a digital image in the inset is 1-M KOH as the electrolyte and separator, and two FeNP@MIL-101(Fe)/CNT composite electrode coatings are posted together. Afterward, the electrode was charged by connecting it to a potentiostat. Light-emitting diode (LED) bulbs were lit by using symmetric devices assembled in sequence to demonstrate the practical application of supercapacitors. As shown in Figure 6a, the inset LEDs could stay lit for more than 14 min. Furthermore, cyclic stability is a significant factor in electrochemical performance analysis. The cyclic stabilities of the FeNP@MIL-101(Fe), CNT, and FeNP@MIL-101(Fe)/CNT electrodes were examined by constant charge–discharge cycling at a current density of 1 A g^{-1} for 10,000 cycles. Figure 6b shows the capacitance retentions of the FeNP@MIL-101(Fe)/CNT composite (95%), CNT (43%), and FeNP@MIL-101(Fe) (56%). The excellent stability of the FeNP@MIL-101(Fe)/CNT electrode originates from the porous assembly, which could improve the lattice sites and volume extension. The minor variation in SC could be attributed to the limited active material shedding from the electrode.[53] The remarkable performance of FeNP@MIL-101(Fe)/CNT is due to the synergistic outcome of its structure, phase alignment, porous structure, and intrinsic resistance. Consequently, the applications of FeNP@MIL-101(Fe)/CNT as a supercapacitor electrode material can be extremely broad. The nanopores of the active materials can increase the wettability of electrolyte/electrode materials, increase the number of dynamic sites of the electrode, and migrate its volume expansion. It also increases the speed of the moving charge and the capacity of the supercharger. In addition, the large surface area of the FeNP@MIL-101(Fe)/CNT composite can produce extra active sites and adsorption/desorption exteriors for the electrolyte, thereby enhancing the electrochemical performance of supercapacitors.

CONCLUSIONS

A unique FeNP@MIL-101(Fe)/CNT composite with a large surface area and suitable channel conductivity for ion transport was used for an electrode materialwith a conductive CNT by facile self-assembly methods. A large effective surface area and suitably high channel conductivity for ion transport have been achieved by making up an electrode material based on a CNT matrix through the self-assembly method. The encapsulation of the FeNP@MIL-101(Fe) crystal on the CNT surfaces, along with its redox-active metal centers, induced pseudocapacitance, enhancing the specific capacitance value. Prominently enhanced cycling stability, effective capacitance, and rapid charge/discharge capability have been demonstrated by the novel electrode with FeNP@MIL-101(Fe)/CNT nanocomposites. The nanocomposite electrode exhibited plausible capacitance retention of 95% after 10,000 cycles, with a calculated gravimetric specific capacitance of 1305 F g^{-1} at a current density of 1 A g^{-1}, revealing an extended cycling life. The symmetric supercapacitor device showed high energy and power density values of 9000 Wh kg^{-1} and 98.65 W kg^{-1}, respectively, highlighting its versatility for various applications.

EXPERIMENTAL SECTION

Materials. Graphite (99.995+% purity) potassium chlorate, ($KClO_3$), nitric acid (HNO_3), and sulfuric acid (H_2SO_4) from Sigma-Aldrich, benzene-1,4-dicarboxylic acid (H_2BDC), *N*,*N*-dimethylformamide (DMF), polyvinylpyrrolidone (PVP), and ferric chloride hexahydrate ($FeCl_3{\cdot}6H_2O$) were purchased from Sinopharm. We used analytical-grade chemical reagents and deionized water for the preparation of aqueous solutions.

Synthesis of Pure Carbon Nanotubes (CNTs). Graphite, potassium chlorate ($KClO_3$), sulfuric acid (H_2SO_4), and nitric acid (HNO_3) were our beginning materials. Initially, 5.0 g of graphite powder was slowly added to fuming nitric acid (HNO_3-25 mL) and sulfuric acid (H_2SO_4-50 mL) for 30 min. After that, we took an ice bath to cool down the mixture. In the ice bath, the solution was cooled down to 5 °C, and 25.0 g of potassium chlorate was added slowly while stirring for 30 min. We took extra precautions at this stage because adding potassium chlorate to the mixture generated a lot of heat. The mixture was heated up to 70 °C for 24 h and then kept in ambient conditions for 3 days. However, some reacting carbons were floating, and the majority of the graphite precipitated to the bottom. Instantly, the floating carbon was poured into 1 L of DI water and stirred for 1 h. After stirring, the solution was immediately filtered and dried. The preceding processes were then carried out four more times. The Staudenmaier approach used to generate graphite oxide and the previously described method used to prepare CNT are comparable.[31,32,56,57] Then, floating graphite was filtered and interacted with potassium chlorate, in contrast to the Staudenmaier procedure that filters all graphite granules.

https://doi.org/10.1021/acsomega.4c00590
ACS Omega 2024, 9, 24546–24557

Synthesis of the FeNP@MIL-101(Fe) Nanocrystal. For the synthesis of porous metal−organic framework material FeNP@MIL-101(Fe), a straightforward solvothermal technique was used.[58] The synthesis approach was to combine 2.026 g $FeCl_36H_2O$ (7.5 mmol), and 0.622 g H_2BDC (4.02 mmol), to 50 mL of DMF. After that, the mixture was ultrasonically treated for 15 min. This DMF mixture was further transferred to a Teflon-lined autoclave and heated at 120 °C for 24 h. After cooling to room temperature, the precipitate was collected and washed with water and ethanol several times. Finally, the obtained material was dried at 60 °C under vacuum for 24 h.

Synthesis of the FeNP@MIL-101/CNT Composite. In brief, 25.2 mg of $FeCl_36H_2O$ and 27.2 mg of CNT were mixed in 20 mL of DMF followed by ultrasonication for 40 min. Afterward, 8.2 mg of H_2BDC and 10 mL of DMF were added drop-wisely to the solution. Subsequently, the mixture was moved to a Teflon-lined autoclave and heated at 120 °C for 24 h. After applying the solvothermal process, the resultant mixture was washed several times with DMF and ethanol. And then, resultant materials were vacuum-dried overnight at 60 °C.

Instruments for Characterization. Using JEM-2100F equipment, transmission electron microscopy (TEM) was conducted (Jeol, Tokyo, Japan). X-ray diffractometer (D/max-2600PC; Rigaku, Tokyo, Japan) has been applied to acquire X-ray diffraction (XRD) patterns. A Fourier-transform infrared spectrometer (FTIR) was used to identify the functional groups of the synthesized material (Band 100; PerkinElmer, Waltham, MA, USA). An X-ray photoelectron spectrometer was used to conduct X-ray photoelectron spectroscopy (XPS) (K-alpha; Thermo Fisher Scientific, MA, USA). A CHI760E potentiostat was used to conduct the electrochemical measurements.

■ ASSOCIATED CONTENT

Supporting Information

The Supporting Information is available free of charge at https://pubs.acs.org/doi/10.1021/acsomega.4c00590.

Set of additional characterizations, statistical study on nanopore sizes, schematic of the energy storage mechanism, and comparison of supercapacitor performance in the context of previous reports (PDF)

■ AUTHOR INFORMATION

Corresponding Author

Seongjae Cho − *Department of Electronic and Electrical Engineering, Ewha Womans University, Seoul 03760, Republic of Korea;* orcid.org/0000-0001-8520-718X; Phone: +82-2-3277-3512; Email: felixcho@ewha.ac.kr

Authors

Hansa Mahajan − *Department of Electronic and Electrical Engineering, Ewha Womans University, Seoul 03760, Republic of Korea;* orcid.org/0000-0003-1393-4518

Arati Kumari Shah − *Department of Electronic and Electrical Engineering, Ewha Womans University, Seoul 03760, Republic of Korea*

Soomin Kim − *Department of Electronic and Electrical Engineering, Ewha Womans University, Seoul 03760, Republic of Korea*

Complete contact information is available at: https://pubs.acs.org/10.1021/acsomega.4c00590

Author Contributions

H.M. conducted the experimental parts including device fabrication and electrochemical analysis and wrote the initial manuscript. A.K.S. helped arrange the experimental results and conveyed the graphical demonstration in part. S.K. validated the graphical representations of the experimental results in the analytical manner. Prof. S.C. initiated the research direction under a government research project, validated the experimental and numerical analysis results, and revised the manuscript.

Funding

This work was supported by National R&D Program through the National Research Foundation of Korea (NRF) funded by the Ministry of Science and ICT (MSIT) under Grant 2021M3H4A6A01048300.

Notes

The authors declare no competing financial interest.

■ ACKNOWLEDGMENTS

This work was supported by National R&D Program through the National Research Foundation of Korea (NRF) funded by the Ministry of Science and ICT (MSIT) under Grant 2021M3H4A6A01048300.

■ REFERENCES

(1) Basim, M.; Ain, Q. U.; Shehzad, K.; Shah, S. A. A.; Jang, B.; Pu, Y. G.; Yoo, J.-M.; Lee, K. Y. A Comprehensive Review on High-efficiency RF-DC Converter for Energy Harvesting Applications. *J. Semicond. Technol. Sci.* **2022**, *22*, 304−325.

(2) Song, Z.; Hofmann, H.; Li, J.; Hou, J.; Han, X.; Ouyang, M. Energy Management Strategies Comparison for Electric Vehicles with Hybrid Energy Storage System. *Appl. Energy* **2014**, *134*, 321−331.

(3) Liu, S.; Fan, W.; Guo, H.; Wu, X.; Chen, J.; Liu, Z.; Wang, X. Relationship between the N_2O Decomposition and NO Formation in $H_2O/CO_2/NH_3$/NO Atmosphere under the Conditions of Simulated Air-Staged Combustion in the Temperature Interval of 900−1600 °C. *Energy* **2020**, *211*, No. 118647.

(4) Ansari, S.; Choudhary, R. B.; Gupta, A. Nanoflower copper sulfide intercalated reduced graphene oxide integrated polypyrrole nano matrix as robust symmetric supercapacitor electrode material. *J. Energy Storage* **2023**, *59*, No. 106446.

(5) Xu, P.; Wei, B.; Cao, Z.; Zheng, J.; Gong, K.; Li, F.; Yu, J.; Li, Q.; Lu, W.; Byun, J.-H.; et al. Stretchable Wire-Shaped Asymmetric Supercapacitors Based on Pristine and MnO_2 Coated Carbon Nanotube Fibers. *ACS Nano* **2015**, *9*, 6088−6096.

(6) She, Z.; Ghosh, D.; Pope, M. A. Decorating Graphene Oxide with Ionic Liquid Nano droplet: an Approach Leading to Energy Dense, High-Voltage Supercapacitors. *ACS Nano* **2017**, *11*, 10077−10087.

(7) Choudhary, R. B.; Ansari, S. Mesoporous complexion and multi-channeled charge storage action of PIn-rGO-TiO_2 ternary hybrid materials for supercapacitor applications. *J. Energy Storage* **2022**, *46*, No. 103912.

(8) Li, N.; Huang, G. W.; Li, Y. Q.; Xiao, H. M.; Feng, Q. P.; Hu, N.; Fu, S. Y. Enhanced Microwave Absorption Performance of Coated Carbon Nanotubes by Optimizing the Fe_3O_4 Nanocoating Structure. *ACS Appl. Mater. Interfaces* **2017**, *9*, 2973−2983.

(9) Xu, X.; Cao, R.; Jeong, S.; Cho, J. Spindle-like Mesoporous α-Fe_2O_3 Anode Material Prepared from MOF Template for High-Rate Lithium Batteries. *Nano Lett.* **2012**, *12* (9), 4988−4991.

(10) Zhang, S.; Wang, K.; Chen, H.; Liu, H.; Yang, L.; Chen, Y.; Li, H. ZIF-67 Derived in-Situ Grown N−Co_3S_4-GN/CNT Interlinked Conductive Networks for High-Performance Especially Cycling Stable Supercapacitors. *Carbon* **2022**, *194*, 10−22.

(11) Chen, Y.; Zhou, Y.; Wang, H.; Lu, J.; Uchida, T.; Xu, Q.; Yu, S.; Jiang, H. Multifunctional PdAg@MIL-101 for one-pot Cascade reaction: Combination of Host-Guest cooperation and bimetallic synergy in catalysis. *ACS Catal.* **2015**, *5*, 2062−2069.
(12) Cai, Y.; Shen, J.; Ge, G.; Zhang, Y.; Jin, W.; Huang, W.; Shao, J.; Yang, J.; Dong, X. Stretchable Ti_3C_2Tx MXene/Carbon Nanotube Composite Based Strain Sensor with Ultrahigh Sensitivity and Tunable Sensing Range. *ACS Nano* **2018**, *12*, 56−62.
(13) Xiao, H.; Wu, Z. S.; Chen, L.; Zhou, F.; Zheng, S.; Ren, W.; Cheng, H. M.; Bao, X. One-Step Device Fabrication of Phosphorene and Graphene Interdigital Micro-Supercapacitors with High Energy Density. *ACS Nano* **2017**, *11*, 7284−7292.
(14) Peng, W.; Song, N.; Su, Z.; Wang, J.; Chen, K.; Li, S.; Wei, B.; Luo, S.; Xie, A. Two-Dimensional MoS_2/Mn-MOF/Multi-Walled Carbon Nanotubes Composite Material for High-Performance Supercapacitors. *Microchem. J.* **2022**, *179*, No. 107506.
(15) Majid, S.; Ali, A. S. G.; Cao, W. Q.; Reza, R.; Ge, Q. Biomass-Derived Porous Carbons as Supercapacitor Electrodes-A Review. *New Carbon Mater.* **2021**, *3*, 546−572.
(16) Cui, J.; Yin, J.; Meng, J.; Liu, Y.; Liao, M.; Wu, T.; Dresselhaus, M.; Xie, Y.; Wu, J.; Lu, C.; Zhang, X. Supermolecule Cucurbituril Subnanoporous Carbon Supercapacitor (SCSCS). *Nano Lett.* **2021**, *21*, 2156−2164.
(17) Sui, Q.; Yu, Y.; Xiang, C.; Wang, Q.; Sun, L.; Xu, F.; Zhang, J.; Zou, Y. Static Adsorption of MOFs Nanosheets on 3D Nanocubes for Supercapacitor Electrode Materials. *J. Alloys Compd.* **2022**, *921*, No. 165982.
(18) Cheng, Y.; Lu, S.; Zhang, H.; Varanasi, C. V.; Liu, J. Synergistic Effects from Graphene and Carbon Nanotubes Enable Flexible and Robust Electrodes for High-Performance Supercapacitors. *Nano Lett.* **2012**, *12*, 4206−4211.
(19) Zhang, W.; Li, M.; Zhong, L.; Huang, J.; Liu, M. A Family of MOFs@Wood-Derived Hierarchical Porous Composites as Free-standing Thick Electrodes of Solid Supercapacitors with Enhanced Areal Capacitances and Energy Densities. *Mater. Today Energy* **2022**, *24*, No. 100951.
(20) Yang, C.; Tang, Y.; Tian, Y.; Luo, Y.; He, Y.; Yin, X.; Que, W. Achieving of Flexible, Free-Standing, Ultra-compact Delaminated Titanium Carbide Films for High Volumetric Performance and Heat-Resistant Symmetric Supercapacitors. *Adv. Funct. Mater.* **2018**, *28*, No. 1705487.
(21) Yao, B.; Peng, H.; Zhang, H.; Kang, J.; Zhu, C.; Delgado, G.; Byrne, D.; Faulkner, S.; Freyman, M.; Lu, X.; Worsley, M. A.; Lu, J. Q.; Li, Y. Printing Porous Carbon Aerogels for Low-Temperature capacitors. *Nano Lett.* **2021**, *21*, 3731−3737.
(22) Krishnan, S.; Gupta, A. K.; Singh, M. K.; Guha, N.; Rai, D. K. Nitrogen-Rich Cu-MOF Decorated on Reduced Graphene Oxide Nanosheets for Hybrid Supercapacitor Applications with Enhanced Cycling Stability. *Chem. Eng. J.* **2022**, *435*, No. 135042.
(23) Xia, Q. X.; Shinde, N. M.; Zhang, T.; Yun, J. M.; Zhou, A.; Mane, R. S.; Mathur, S.; Kim, K. H. Seawater Electrolyte-Mediated High Volumetric MXene-Based Electrochemical Symmetric Supercapacitors. *Dalton Trans.* **2018**, *47*, 8676−8682.
(24) Ullah, S.; Khan, I. A.; Choucair, M.; Badshah, A.; Khan, I.; Nadeem, M. A. A Novel Cr_2O_3-Carbon Composite as a High-Performance Pseudo-Capacitor Electrode Material. *Electrochem. Acta.* **2015**, *171*, 142−149.
(25) Jang, D. J.; Ryu, H.; Cha, H.; Lee, N.-Y.; Kim, Y.; Kwon, M.-W. Synaptic Device based on Resistive Switching Memory using Single-Walled Carbon Nanotubes. *J. Semicond. Technol. Sci.* **2022**, *22*, 346−352.
(26) Kaempgen, M.; Chan, C. K.; Ma, J.; Cui, Y.; Gruner, G. Printable Thin Film Supercapacitors Using Single-Walled Carbon Nanotubes. *Nano Lett.* **2009**, *9*, 1872−1876.
(27) Sharma, M.; Adalati, R.; Kumar, A.; Chawla, V.; Chandra, R. Single-Step Fabrication of Nanostructured Cr_2O_3-MoO_2 Composite Flexible Electrode for Top-Notch Asymmetric Supercapacitor. *Appl. Surf. Sci.* **2021**, *555*, No. 149721.
(28) Hu, C. C.; Chang, K. H.; Lin, M. C.; Wu, Y. T. Design and Tailoring of the Nano tubular Arrayed Architecture of Hydrous RuO_2 for next Generation Supercapacitors. *Nano Lett.* **2006**, *6*, 2690−2695.
(29) Song, Z.; Li, J.; Han, X.; Xu, L.; Lu, L.; Ouyang, M.; Hofmann, H. Multi-Objective Optimization of a Semi-Active Battery/Supercapacitor Energy Storage System for Electric Vehicles. *Appl. Energy* **2014**, *135*, 212−224.
(30) Qi, J.; Wang, D.; Zhang, Z.; Hu, R.; Sui, Y.; He, Y.; Meng, Q.; Wei, F. Enhanced Performance of Mesoporous $NiCo_2S_4$ Nanosheets Fiber-Shaped Electrode for Supercapacitor. *Micro & Nano Lett.* **2021**, *16*, 263−267.
(31) Jiang, Y.; Wang, Z.; Huang, J.; Yan, F.; Du, Y.; He, C.; Liu, Y.; Yao, G.; Lai, B. A Singlet Oxygen Dominated Process through Photo catalysis of CuS-Modified MIL-101(Fe) Assisted by Peroxymonosulfate for Efficient Water Disinfection. *Chem. Eng. J.* **2022**, *439*, No. 135788.
(32) Xue, Y.; Zheng, S.; Xue, H.; Pang, H. Metal-Organic Framework Composites and Their Electrochemical Applications. *J. Mater. Chem. A* **2019**, *7*, 7301−7327.
(33) Skobelev, I. Y.; Sorokin, A. B.; Kovalenko, K. A.; Fedin, V. P.; Kholdeeva, O. A. Solvent-free allylic oxidation of alkenes with O_2 mediated by Fe- and Cr-MIL-101. *J. Catal.* **2013**, *298*, 61−69.
(34) Oh, H. J.; Kim, S. Preparation and Capacitive Property of Graphene Oxide Composite Supercapacitor Electrodes Functionalized by Fe-Based Metal-Organic Frameworks. *Carbon Lett.* **2022**, *32*, 273−283.
(35) Liu, Z.; He, W.; Zhang, Q.; Shapour, H.; Bakhtari, M. F. Preparation of a GO/MIL-101 (Fe) Composite for the Removal of Methyl Orange from Aqueous Solution. *ACS omega* **2021**, *6*, 4597−4608.
(36) Gao, J.; He, P.; Yang, T.; Wang, X.; Zhou, L.; He, Q.; He, X. Short Rod-like Ni-MOF Anchored on Graphene Oxide Nanosheets: A Promising Voltammetric Platform for Highly Sensitive Determination of p-chloronitrobenzene. *J. Electroanal. Chem.* **2020**, *861*, No. 113954.
(37) Ullah, S.; Bustam, M. A.; Al-Sehemi, A. G.; Assiri, M. A.; Kareem, F. A. A.; Mukhtar, A.; Gonfa, G. Influence of Post-synthetic Graphene Oxide (GO) Functionalization on the Selective CO_2/CH_4 Adsorption Behavior of MOF-200 at Different Temperatures; An Experimental and Adsorption Isotherms Study. *Microporous Mesoporous Mater.* **2020**, *296*, No. 110002.
(38) Yan, D.; Hu, H.; Gao, N.; Ye, J.; Ou, H. Fabrication of Carbon Nanotube Functionalized MIL-101 (Fe) for Enhanced Visible-light Photo-catalysis of Ciprofloxacin in Aqueous Solution. *Appl. Surf. Sci.* **2019**, *498*, No. 143836.
(39) Zhuang, J. L.; Liu, X. Y.; Mao, H. L.; Wang, C.; Cheng, H.; Zhang, Y.; Du, X.; Zhu, S.; Ren, B. Hollow Carbon Polyhedra Derived from Room Temperature Synthesized Iron-Based Metal-Organic Frameworks for Supercapacitors. *J. Power Sources* **2019**, *429*, 9.
(40) Li, J.; Wang, L.; Liu, Y.; Zeng, P.; Wang, Y.; Zhang, Y. Removal of Berberine from Wastewater by MIL-101(Fe): Performance and Mechanism. *ACS Omega* **2020**, *5*, 27962−27971.
(41) Zhuannian, L.; Wenwen, H.; Qingyun, Z.; Habiba, S.; Mohammad, B. Preparation of a GO/MIL-101(Fe) composite for the removal of Methyl orange from aqueous solution. *ACS Omega* **2021**, *6* (7), 4597−4608.
(42) Noorpoor, Z.; Pakdehi, S. G.; Rashidi, A. High capacity and energy-efficient dehydration of liquid fuel 2-dimethyl amino ethyl-azide (DMAZ) over chromium terephthalic (MIL-101) nano adsorbent. *Adsorption* **2017**, *23*, 743−752.
(43) Xie, J.; Ma, R.; Fang, H.; Shi, H.; Liu, D. MIL-101(Fe)-Attached Graphene Oxide for High-Performance Supercapacitors with Sound Stability in Acid Electrolyte. *Cryst. Growth Des.* **2022**, *22*, 2997−3006.
(44) Wang, X. H.; Huang, F. F.; Rong, F.; He, P.; Que, R. H.; Jiang, S. P. Unique MOF-derived Hierarchical MnO_2 Nanotubes@ NiCoLDH/CoS_2 Nanocage materials as High-performance Supercapacitors. *J. Mater. Chem. A* **2019**, *7*, 12018−12028.

https://doi.org/10.1021/acsomega.4c00590
ACS Omega 2024, 9, 24546−24557

(45) Tittaya, B.; Rodjana, B. Evaluation of metal-organic framework NH_2-MIL-101(Fe) as an efficient sorbent for dispersive micro-solid phase extraction of phenolic pollutants in environmental water samples. *Heliyon* **2019**, *5*, No. e02848.
(46) Deyi, Y.; Han, H.; Naiyum, G.; Jinshao, Y.; Huase, O. Fabrication of carbon nanotube of functionalized MIL-101(Fe) for enhanced visible-light photocatalysis of ciprofloxacin in aqueous solution. *Appl. Surf. Sci.* **2019**, *498*, No. 143836.
(47) Kuang, M.; Li, T. T.; Chen, H.; Zhang, S. M.; Zhang, L. L.; Zhang, Y. X. Hierarchical $Cu_2O/CuO/Co_3O_4$ Core-shell Nanowires: Synthesis and Electrochemical Properties. *Nanotechnology* **2015**, *26*, No. 304002.
(48) Lee, C.; Kim, S. K.; Choi, J.-H.; Chang, H.; Jang, H. D. Electrochemical performance of iron-cobalt oxides nanoparticles loaded crumpled graphene for supercapacitor. *J. Alloys Compd.* **2018**, *735*, 2030−2037.
(49) Mazloum-Ardakani, M.; Sabaghian, F.; Yavari, M.; Ebady, A.; Sahrale, N. Enhance the performance of iron oxide nanoparticles in supercapacitor applications through internal contact of α-Fe_2O_3@ CeO_2 core-shell. *J. Alloys Compd.* **2020**, *819*, No. 152949, DOI: 10.1016/j.jallcom.2019.152949.
(50) Sun, H.; Zheng, L.; Xi, Y.; Zhai, S.; An, Q.; Xiao, Z. Nickel-iron sulfide nanoparticles supported on biomass-derived N-doped hierarchical porous carbon as a robust electrode for supercapacitors. *Electrochim. Acta* **2023**, *466*, No. 143053, DOI: 10.1016/j.electacta.2023.143053.
(51) Huang, D.; Chen, L.; Yue, L.; Yang, F.; Guo, H.; Yang, W. Nitrogen-doped carbon-enriched MOF and derived hierarchical carbons as electrode for excellent asymmetric aqueous supercapacitor. *J. Alloys Compd.* **2021**, *867*, No. 158764, DOI: 10.1016/j.jallcom.2021.158764.
(52) Wang, L.; Yao, H.; Chi, F.; Yan, J.; Cheng, H.; Li, Y.; Qu, L. Spatial-Interleaving Graphene Supercapacitor with High Area Energy Density and Mechanical Flexibility. *ACS Nano* **2022**, *16*, 12813−12821.
(53) Farisabadi, A.; Moradi, M.; Hajati, S.; Kiani, M. A.; Espinos, J. P. Controlled Thermolysis of MIL-101 (Fe, Cr) for the Synthesis of Fe_xO_y/Porous Carbon as the Negative Electrode and Cr_2O_3/Porous Carbon as the Positive Electrode of the Supercapacitor. *Appl. Surf. Sci.* **2019**, *469*, 192−203.
(54) Dai, Y.; Yao, Y.; Li, M.; Fang, X.; Shen, C.; Li, F.; Liu, Y. Carbon Nanotube Filter Functionalized with MIL-101(Fe) for Enhanced Flow-through Electro-Fenton. *Environ. Research* **2022**, *204*, No. 112117.
(55) Yan, D.; Hu, H.; Gao, N.; Ye, J.; Ou, H. Fabrication of Carbon Nanotube Functionalized MIL-101(Fe) for Enhanced Visible-Light Photo catalysis of Ciprofloxacin in Aqueous Solution. *Appl. Surf. Sci.* **2019**, *498*, No. 143836.
(56) Kumar Jagadeesan, A.; Thangavelu, K.; Dhananjeyan, V.Carbon Nanotubes: Synthesis, Properties, and Applications. In *Surface Science - a Handbook*; 2020; p 92995.
(57) Lee, D. W.; Seo, J. W. Preparation of carbon nanotube from graphite powder at room temperature. *Mater. Sci.* **2011**, *1007*, 1062.
(58) Zorainy, M. Y.; Alalm, M. G.; Kaliaguine, S.; Boffito, D. C. Revisiting the MIL-101 metal−organic framework: design, synthesis, modifications, advances, and recent applications. *J. Mater. Chem. A* **2021**, *9*, 22159−22217.

https://doi.org/10.1021/acsomega.4c00590
ACS Omega 2024, 9, 24546−24557